Journal of the Mechanical Behavior of Biomedical Materials 99 (2019) 104–117

Contents lists available at ScienceDirect

Journal of the Mechanical Behavior of Biomedical Materials

journal homepage: www.elsevier.com/locate/jmbbm

Predicting the output dimensions, porosity and elastic modulus of additive manufactured biomaterial structures targeting orthopedic implants

F. Bartolomeu[a,*], J. Fonseca[a], N. Peixinho[b], N. Alves[c], M. Gasik[d], F.S. Silva[a], G. Miranda[a]

[a] Center for MicroElectroMechanical Systems (CMEMS-UMinho), University of Minho, Campus de Azurém, 4800-058, Guimarães, Portugal
[b] Department of Mechanical Engineering, University of Minho, Campus of Azurém, Guimarães, Portugal
[c] Centre for Rapid and Sustainable Product Development Polytechnic Institute of Leiria, Rua General Norton de Matos, Apartado 4133, 2411-901, Leiria, Portugal
[d] Department of Materials Science and Engineering, School of Chemical Technology, Aalto University Foundation, 00076, Aalto, Espoo, Finland

ARTICLE INFO

Keywords:
Selective laser melting
Ti6Al4V
Multi-material
Predictive models
Elastic modulus

ABSTRACT

SLM accuracy for fabricating porous materials is a noteworthy hindrance when aiming to obtain biomaterial cellular structures owing precise geometry, porosity, open-cells dimension and mechanical properties as outcomes. This study provides a comprehensive characterization of seventeen biomaterial Ti6Al4V-based structures in which experimental and numerical investigations (compression stress-strain tests) were carried out. Monomaterial Ti6Al4V cellular structures and multi-material Ti6Al4V-PEEK cellular structures were designed, produced by SLM and characterized targeting orthopedic implants. In this work, the differences between the CAD design and the as-produced Ti6Al4V-based structures were obtained from image analysis and were used to develop predictive models. The results showed that dimensional deviations inherent to SLM fabrication are systematically found for different dimensional ranges. The present study proposes several mathematical models, having high coefficients of determination, that estimate the real dimensions, porosity and elastic modulus of Ti6Al4V-based cellular structures as function of the CAD model. Moreover, numerical analysis was performed to estimate the octahedral shear strain for correlating with bone mechanostat theory limits. The developed models can help engineers to design and obtain near-net shape SLM biomaterials matching the desired geometry, open-cells dimensions, porosity and elastic modulus. The obtained results show that by using these AM structures design it is possible to fabricate components exhibiting a strain and elastic modulus that complies with that of bone, thus being suitable for orthopedic implants.

1. Introduction

Selective Laser Melting is an additive manufacturing layer-wise process able to fabricate 3D components based on computer-aided design (CAD) data (Van Hooreweder et al., 2017; Dai et al., 2016; Bartolomeu et al., 2017a). SLM versatility allows the fabrication of customized and complex geometries such as metallic cellular structures (Xu et al., 2017; Bartolomeu et al., 2017b, 2018a). Ti6Al4V cellular structured materials are capable to exhibit multifunctionality (mechanical, biological, chemical, physical and other) are currently in great demand due to their potential/benefits to be used in several orthopedic implant applications (Bobbert et al., 2017; Wang et al., 2016).

The design of Ti6Al4V cellular structures materials (geometry and resulting porosity) can be prepared focused on the required mechanical properties such as strength and especially stiffness (Weiβmann et al., 2016; Bartolomeu et al., 2017c). Ideally, the design of these materials for implants should be made to obtain the suitable properties according to the anatomical location and the patient, with information obtained by tomography or magnetic resonance imaging 3D data (e.g. hip, dental, tibia, knee) (Chen and Thouas, 2015; Yan et al., 2015; Ryan et al., 2006; Thavornyutikarn et al., 2014).

The accuracy of Selective Laser Melting process for fabricating porous materials is usually limited, with significant differences being detected when comparing CAD design with the produced components (Bagheri et al., 2017; Yan et al., 2012). In fact, dimensional and geometrical divergences on porous materials are frequently detected, especially when the minimum dimensions used are close to the technological limits (Bagheri et al., 2017; Arabnejad et al., 2016). Considering that cellular structures are designed aiming to obtain specific geometry, porosity, open-cells dimension and mechanical properties as outcomes, these deviations are crucial (Bagheri et al., 2017). Different heat transfer phenomena between the area under direct laser scanning

* Corresponding author.
E-mail address: flaviojorgebartolomeu@gmail.com (F. Bartolomeu).

https://doi.org/10.1016/j.jmbbm.2019.07.023
Received 6 February 2019; Received in revised form 18 July 2019; Accepted 20 July 2019
Available online 22 July 2019
1751-6161/

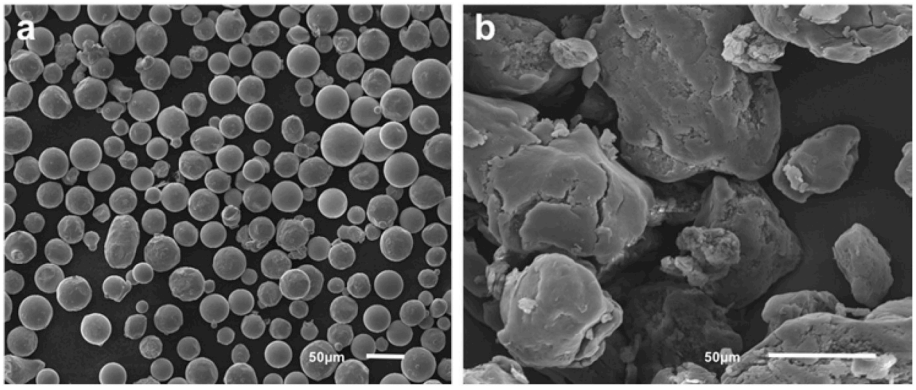

Fig. 1. SEM images of (a) Ti6Al4V and (b) PEEK powders.

and their surrounding powder and also the structures orientation are pointed as possible reasons for these deviations (Bagheri et al., 2017; Dias et al., 2014).

Ti6Al4V dense materials are still being extensively used as dental and orthopedic materials owing to suitable mechanical properties, corrosion resistance, relative low weight and elastic modulus and biological compatibility (Arabnejad et al., 2016; Zhang et al., 2014; Bartolomeu et al., 2016). Nevertheless, two key aspects are still being related to implant failure (Moura et al., 2017). The first consists on the over-high elastic modulus of dense Ti6Al4V (≈110 GPa), as compared to that of natural bone such as cortical (10–30 GPa) and trabecular (≈2 GPa) (Wang et al., 2016; Chen et al., 2017; Fousová et al., 2017; Bose et al., 2018). Moreover, being a self-optimizing structure, bone tissue is capable to adapt to external loading conditions. According to Frost's mechanostat theory the biological response of bone depends on the level of strain exerted (Frost, 2004). Octahedral shear strain is pointed as the most relevant strain for the mechanostat theory and a microstrain between 1500 and 3000 με leads to bone mass formation due to the physiologic demand (Piccinini et al., 2016). The current mismatch found on Ti6Al4V dense implants induces stress shielding, causing bone resorption and finally leading to implant failure (Geetha et al., 2009; Holzwarth and Cotogno, 2012). The second is the modest wear performance of Ti6Al4V material which is reported to play a crucial role in biomedical load-bearing applications due to the inflammatory reactions triggered by the release of metallic ions and wear debris (Bose et al., 2018; Bartolomeu et al., 2018b). By designing Ti6Al4V cellular structures, it is feasible to tailor the mechanical properties as elastic modulus and then obtain customized components suitable for each patient/implantation region. Regarding Ti6Al4V wear resistance, several approaches have been explored, as surface treatments, coatings, composite materials, etc. Particularly, M. Buciumeanu et al. (2018) studied the tribological behavior of Ti6Al4V-PEEK multi-material structures and showed higher wear performance of these structures when compared to Ti6Al4V dense materials produced by conventional routes. These advantages can be used to substantially improve these structures wear resistance by filling their open-cells with PEEK. Poly-ether-ether-ketone (PEEK) is a polymeric material which displays high wear and corrosion resistance, mainly due to its auto lubrication effect (Koike et al., 2012). After confirming its biocompatibility, PEEK has been extensively employed as biomaterials for orthopedic, trauma, and spinal implants (Kurtz and Devine, 2007). F. Bartolomeu et al. (2018b) investigated the tribocorrosion performance of multimaterial Ti6Al4V structures. It was concluded that the introduction of PEEK into TiAl4V cellular structures open-cells decreases the OCP value (lower tendency to corrosion) during sliding and increases the wear resistance. Thus, a multi-material solution that gathers Ti6Al4V and PEEK, besides being able to withstand the loads occurring after implantation is an alternative to fully dense metals hip implants once there are evidences that this solution enhances the wear and tribocorrosion performance (Bartolomeu et al., 2018b; Buciumeanu et al., 2018; Sampaio et al., 2016).

In this study, seventeen types of Ti6Al4V cellular structures were designed and produced by SLM differing only on their unit cell dimensions. Additionally, seventeen types of Ti6Al4V-PEEK multi-material structures were also fabricated. A morphological study allowed to measure the differences between the as-design and the as-produced specimens. This study allowed to create numerical models with adjusted designs for all the specimens. The numerical and the experimental results were then compared. This study proposes mathematical models capable to predict the real elastic modulus and real porosity using as input the model CAD dimensions for a given cubic-like geometry based on the differences measured between the as-design and the as-produced specimens.

2. Experimental details

2.1. Starting materials

Ti6Al4V spherical powder purchased from *SLM Solutions* (Germany), with a D90 diameter of 40 µm was used to fabricated Ti6Al4V Selective Laser Melted specimens. PEEK powder purchased from *Evonik Industries* (Germany) with a D50 diameter of 50 µm, was used to produce multi-material Ti6Al4V-PEEK structures. SEM images present in Fig. 1 show the morphology of the starting powders. Ti6Al4V cast/forged commercial alloy from *Titanium Products Ltd.* (United Kingdom) was also used for comparative purposes, representing the commercial solution currently used in implants.

2.2. Study design

Table 1 aims to resume the fabrication, materials, geometries and the Model CAD design details. All the fabricated specimens have a cylindrical shape with an average diameter of 6 mm and 5 mm height. SP1 corresponds to Ti6Al4V cast/forged dense specimens obtained from Ti6Al4V bar. SP2 corresponds to Ti6Al4V SLM dense specimens. SP3 to SP19 are Ti6Al4V cellular structures (cubic-like structures) produced by SLL and SP3-PEEK to S19-PEEK are Ti6Al4V-PEEK multi-material structures by SLM followed by pressure assisted injection.

In this work, SLM process was used to fabricate Ti6Al4V cellular structured specimens. Model CAD data was prepared accordingly to the defined design presented in Table 1. The cellular structures were modelled with quadrangular open-cells and the distance between two consecutive open-cells was defined as “walls”. In this sense, 18 CAD files were prepared: 1 Ti6Al4V dense specimen (SP2) and 17 Ti6Al4V cellular structures (SP3 to SP19). As a consequence of the differences between these structure's walls and open-cells dimensions (see Table 1), 17 different levels of porosity, from 43.2% (SP3) to 92.3% (SP19) were designed.

Table 1
Processing technology, materials, geometries and model CAD design details for the tested specimens.

Specimen		Processing Technology	Materials and geometry	Model CAD design details		
				Open-cells (μm)	Walls (μm)	Porosity[a]/PEEK[b] percentage
SP1		Casting/Forging	Ti6Al4V Dense	-	-	~0
SP2		SLM		-	-	~0
SP3[a]	SP3-PEEK[b]	SLM[a]	Ti6Al4V cellular structures[a]	350	400	43.2
SP4[a]	SP4-PEEK[b]	SLM and Pressure assisted injection[b]	Ti6Al4V-PEEK multi-material cellular structures[b]	400	400	46.3
SP5[a]	SP5-PEEK[b]			350	350	49.9
SP6[a]	SP6-PEEK[b]			400	350	52.9
SP7[a]	SP7-PEEK[b]			350	300	53.6
SP8[a]	SP8-PEEK[b]			450	350	55.9
SP9[a]	SP9-PEEK[b]			400	300	58.2
SP10[a]	SP10-PEEK[b]			500	400	58.9
SP11[a]	SP11-PEEK[b]			500	350	61.7
SP12[a]	SP12-PEEK[b]			450	300	62.5
SP13[a]	SP13-PEEK[b]			500	300	65.2
SP14[a]	SP14-PEEK[b]			600	350	66.7
SP15[a]	SP15-PEEK[b]			600	300	71.8
SP16[a]	SP16-PEEK[b]			500	150	83.3
SP17[a]	SP17-PEEK[b]			600	150	87.0
SP18[a]	SP18-PEEK[b]			500	100	90.7
SP19[a]	SP19-PEEK[b]			600	100	92.3

[a] For Ti6Al4V structures made by SLM.
[b] For Ti6Al4V-PEEK structures made by SLM followed by Pressure Assisted Injection.

2.3. Fabrication details

Fig. 2 aims to illustrate the processing route of SLM technique. Firstly, 3D CAD *SolidWorks software* was used for modeling all the SLM specimens investigated in this study. *Materialise Magics software* tools were used to generate the supports of the specimens which, in this case, correspond to the first 2 mm of production and are particularly important to assure a suitable heat flow. Then, *.stl* files (contemplating supports and specimen) are incorporated into *SLM Autofab software*, capable to implement a numerical slicing of the supports and specimens defining each layer for fabrication. After assuring all the preparation protocols according to SLM Solutions specifications, the fabrication occurs until the last layer is reached.

F. Bartolomeu et al. (Bartolomeu et al., 2016) reported a processing parameters optimization study regarding Ti6Al4V materials produced using the same SLM equipment. The processing parameters that were used in this study were defined based on the abovementioned investigation where the most effective parameters were obtained. In this sense, the processing parameters used to fabricate the Ti6Al4V specimens of the present study were as follows: 90W of laser power, 600 mm/s of scan speed, 80 μm of scan spacing (distance between two consecutive laser scans) and 30 μm of layer thickness. Using the Ti6Al4V cellular structures previously produced by SLM, Ti6Al4V-PEEK specimens were produced by means of pressure assisted injection. PEEK was forced to fill the cellular structures open-cells by applying pressure and temperature simultaneously. As shown in Fig. 3, after placing Ti6Al4V cellular specimens in a steel mold, PEEK powder is introduced. A top punch is then inserted in the mold and the all system is positioned in a chamber with a controlled atmosphere (vacuum of 10^2 mbar) and a residual pressure was applied to accommodate PEEK powder. Induction was used to heat the system using a heating rate around 80 °C/min until reaching 380 °C (approximately 35 °C above PEEK melting point). This temperature is controlled using a thermocouple type Z placed in the mold very close to the specimen. The induction is then stopped until the

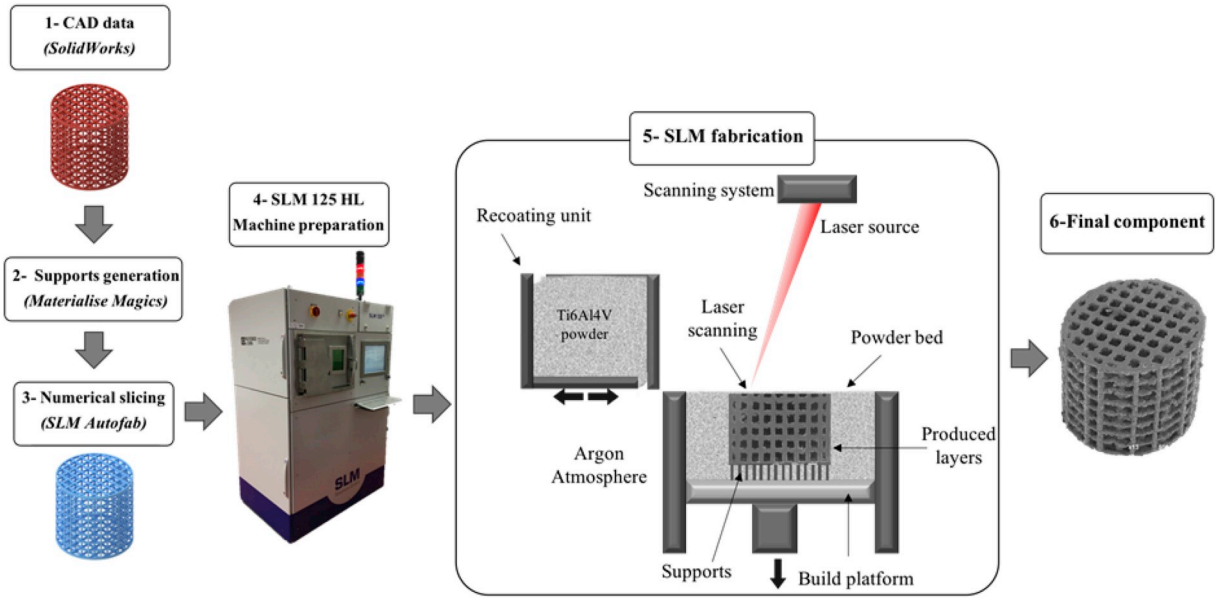

Fig. 2. Schematic representation of SLM technique from CAD data to final component.

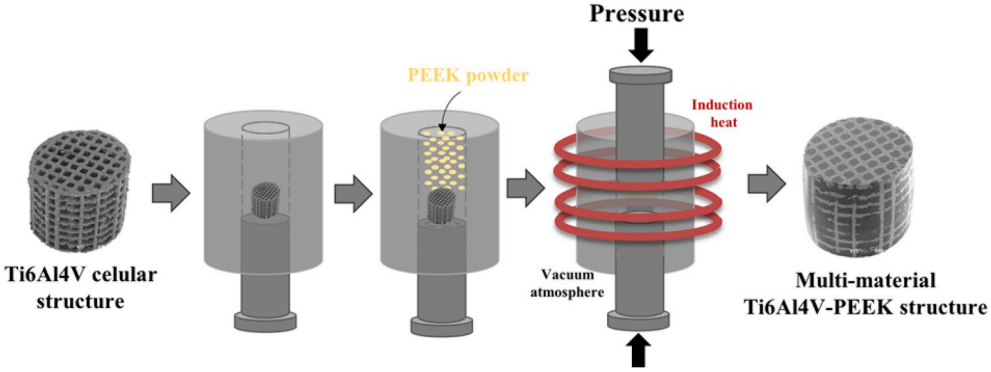

Fig. 3. Pressure assisted injection procedure details for Ti6Al4V-PEEK fabrication.

temperature decreases until 300 °C and in that moment a pressure of 25 MPa is applied during 5 s. This pressure forces PEEK to fill the open-cells. Induction heating is turned on again and this cycle is repeated to assure a complete filling. Finally, after reaching a manageable temperature the Ti6Al4V-PEEK multi-material structures are removed from the mold.

2.4. Mechanical testing

In order to obtain the elasticity modulus of the Ti6Al4V and Ti6Al4V-PEEK multi-material structures, compression tests were performed. For each condition, at least three tests were performed in three different specimens. The compression tests were made by using a universal servo hydraulic testing equipment (Instron 8874, USA) at room temperature according to ISO 13314 standard. The load gauge of the equipment was used for the load signal acquisition. The compression tests were performed with a crosshead speed of 0.005 mm/s and the strain signal was obtained using a dynamic extensometer from Instron (model 2620-601) which was designed according to ISO 9513 standard. Fig. 4 shows typical stress-strain curves for four Ti6Al4V cellular structures and also for dense Ti6Al4V. These curves show the linear elastic regimes under compression for different levels of porosity being similar to the behavior reported elsewhere (Stamp et al., 2009; Ashby, 2006).

2.5. Numerical analysis: geometrical model, boundary conditions and mesh grid

Finite element analysis software *COMSOL Multiphysics* was used to simulate compression stress-strain tests. Mono-material Ti6Al4V cellular structures and Ti6Al4V-PEEK multi-material structures models were used. A structural mechanical module was set for the mechanics simulation for different cellular structures. Hooke's law for linear elasticity was used.

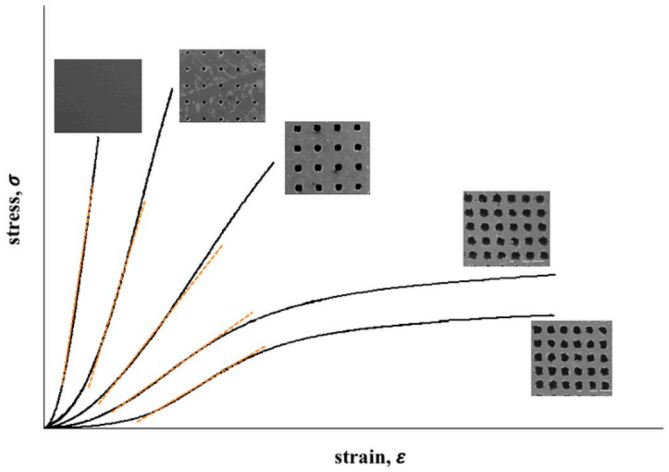

Fig. 4. Typical stress-strain curves obtained for four Ti6Al4V structures tested and for dense Ti6Al4V.

The mono-material Ti6Al4V structures were modelled as a linear elastic material (Ti6Al4V) with an elastic modulus of 110 GPa, a Poisson's ratio of 0.34 and density of 4500 kg/m^3 (Chen and Thouas, 2015; Rotta and Seramak, 2015). The multi-material Ti6Al4V-PEEK structures were modelled, also, as a linear elastic material considering an elastic modulus of 3.76 GPa, a Poisson's ratio of 0.38 and a density of 1300 kg/m^3 as PEEK properties (Garcia-Gonzalez et al., 2015). A load force (F) was applied on the nodes of the upper surface of the model. The effective elastic modulus (E_f) was calculated using the following equation:

$$E_f = \frac{F}{A_0} \times \frac{L_0}{\Delta L} \quad (1)$$

where F is the load force, $A_0$is the initial area of the scaffold, and the axial strain, $\varepsilon = \left(\frac{\Delta L}{L_0}\right)$.

Fig. 5 shows the numerical analysis details and intents to highlight the geometrical model, the boundary conditions and the mesh grid conditions defined in the study.

Tetrahedral elements were used as the mesh element types for all the numerical models. The number of elements and the DOF'S (degrees of freedom) was varying from simulation to simulation. However, in all simulations the same rational was used to generate the mesh. Two parameters were created, h_0 (starting element size) and h_d (element size divider), and the maximum element size was expressed in terms of h_0/h_d and the minimum element size in $(h_0/h_d) \times 0.25$. Mesh converge analysis was carried out for all the numerical analysis through a parametric study where h_d was varying aiming to assure the convergence of the numerical simulation. A quarter of the total cellular structures specimens was used to simplify the model and reduce the consequent time consumption, whilst decreasing the degrees of freedom. In this sense, the blue faces depicted in Fig. 5 represent the symmetry planes of the cellular structures. In this faces the displacement were constrained (equaling zero) in the normal direction to them.

2.6. Morphological analysis

Scanning Electron Microscopy (FEI Nova 200) was used to obtained SEM images for all the Ti6Al4V cellular structures and Ti6Al4V-PEEK multi-material structures, acquiring isometrical, top and cross-sections views of these structures, as seen in Figs. 6–9.

The quantitative morphological analysis performed in this study considered 2D surface images (top views of the SLM structures) as input data, once these were considered representative of the general bulk of the structure. Adobe Photoshop software was used to perform the

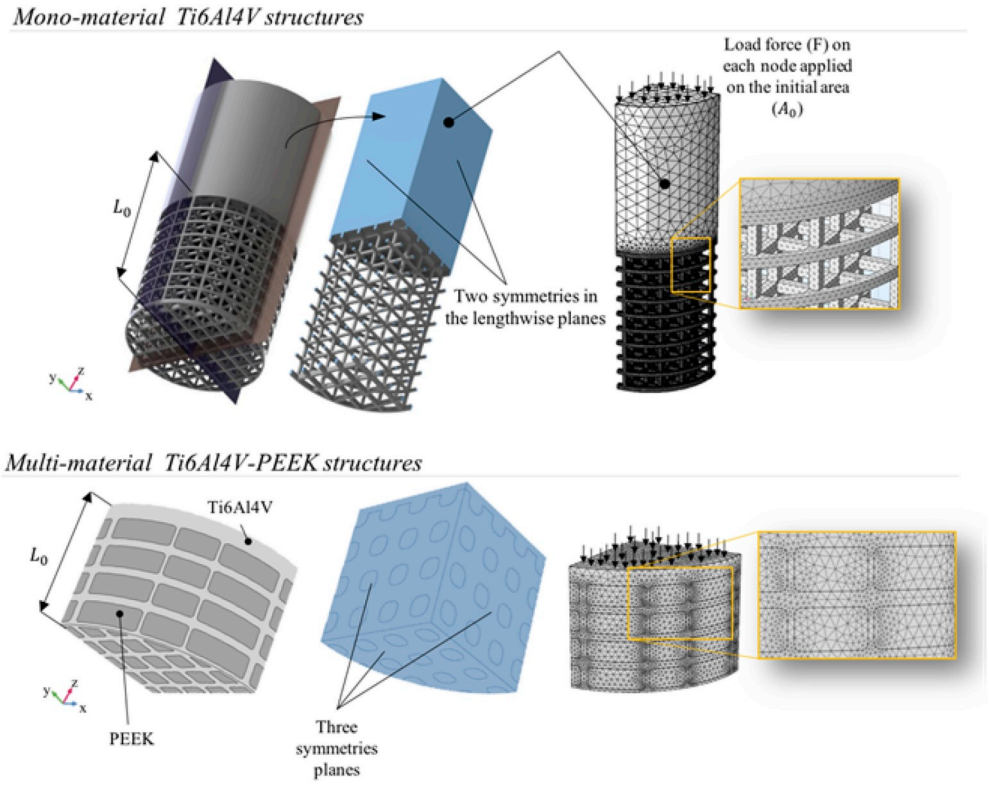

Fig. 5. Numerical analysis details of the COMSOL Multiphysics compression stress-strain tests.

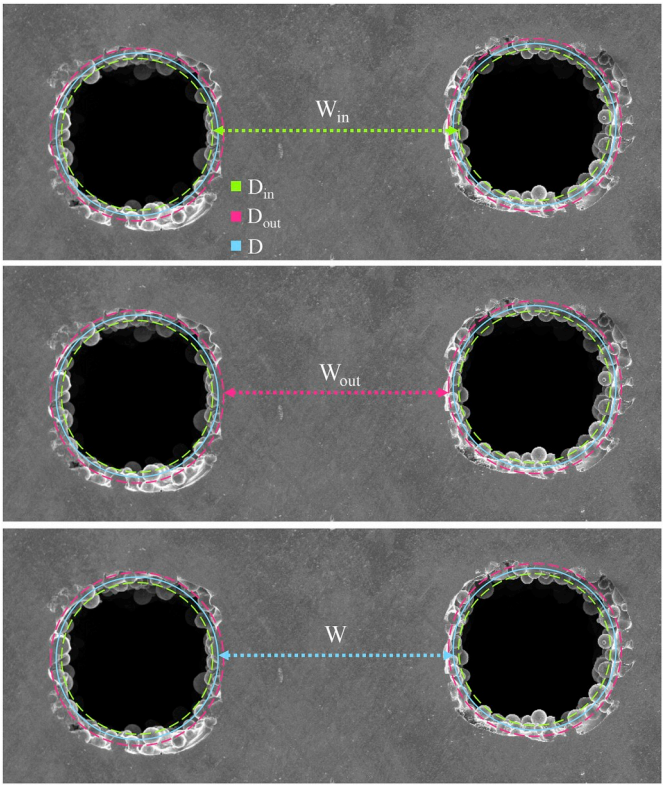

Fig. 6. Methodology adopted to perform the measurements of the open-cells and the walls dimensions.

morphological analysis using these SEM images, systematically measuring the open-cells and the walls (distance between two consecutive open-cells) dimensions (see Fig. 6). The dimension of the open-cells (d and h) and walls (W) were obtained, as exemplified in Fig. 6. For obtaining the average dimensions, three different images from three different specimens were analyzed for each condition (SP3 to SP19). To sum, for each condition, a total of 60 measurements were made, namely on 30 open-cells and 30 walls.

In respect to the open-cell, the parameters D_{in} and D_{out} were measured as the inner and the outer dimensions (Fig. 6). Using the same rational, W_{in} and W_{out} were also measured as the distance between two consecutive D_{in} and D_{out}, respectively. For each measurement, the parameter D was calculated as the average between D_{in} and D_{out}. The parameter W was calculated as the average between W_{in} and W_{out}.

After understanding that the differences between the Model CAD and the SLM produced structures are non-negligible, new CAD designs (hereafter named adjusted CAD designs) were created aiming to reproduce the real dimensions and geometries of the produced structures. Fig. 7 presents the method used in this study, showing that some of the open-cells of these structures were better approximated by circumferences (from specimen SP3 till SP13) while others were better approximated by squares with filleted vertices (SP14 to SP19).

This morphological analysis was judiciously made for having a reproducible method, and for allowing to detect unusual micro-details as micro-defects, that are outliers that must be disregarded.

3. Results and discussion

3.1. Characterization prior to the mechanical testing

In this study, SLM technique was used to produce a variety of Ti6Al4V cellular structures with different levels of porosity. Fig. 8 depicts SEM images of SP3, SP10 and SP19 specimens. Specimens SP3 and SP19 correspond to the outmost specimens in terms of model CAD porosity. SP3 has the lowest porosity (43.2%) having open-cells of 350 μm and walls of 400 μm. On the other hand, SP19 has the highest porosity (92.3%) with open-cells of 600 μm and walls of 100 μm SP10 was also analyzed, having a CAD porosity of 58.9% and 500 and

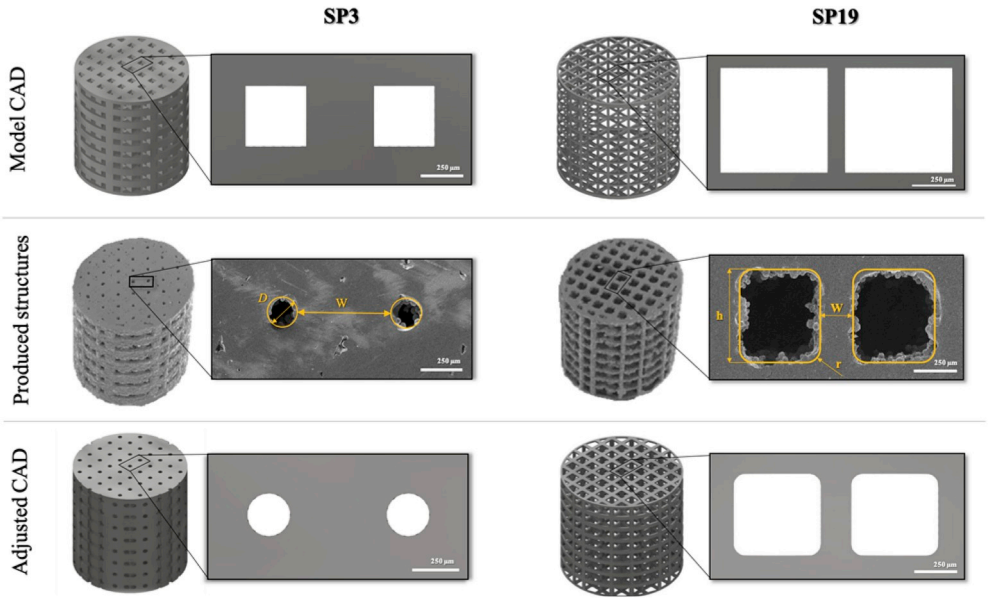

Fig. 7. Comparison between the Model CAD, the produced structures and the Adjusted CAD.

400 μm open-cells and walls respectively.

Fig. 9 depicts SEM images of SP3-PEEK, SP10-PEEK and SP19-PEEK multi-material structures. Regarding these specimens, the porosity of SP3, SP10 and SP19 now corresponds to the percentage of PEEK inside the Ti6Al4V-PEEK multi-material structures. When observing the cross-section views depicted in Fig. 9, the presence of PEEK is noticed through all the open-cells. SP3 is the multi-material structure with the lower porosity and then the most difficult specimen's group to introduce PEEK. Even considering the smallest open-cell (232 μm ± 11), Fig. 9 confirms the efficiency of press assisted injection methodology to introduce PEEK into the Ti6Al4V cellular structures.

By analyzing the SEM images of all the produced specimens, it was possible to measure the dimensions of the open-cells and walls, for all the specimens, as displayed in Table 2. For all the structures, the dimension of the open-cells is, on average, 112 μm ± 8 μm lower compared to the model CAD dimension. On the contrary, it was found that the dimension of the walls, for all the structures, is 100 ± 11 μm higher than the model CAD design. As a consequence of these deviations, a lower porosity of the produced specimens is found when compared to the as-designed (Model CAD) for all the groups.

After obtaining the above-mentioned deviations between the model CAD design and the produced specimens, an adjusted CAD was modelled considering the geometry simplifications explained in section 2.5. Fig. 10 shows some representative examples (SP3, SP11, SP18 and SP19) regarding the differences between the model CAD, the produced specimens and the adjusted CAD.

The porosity of the as-designed (Model CAD), the experimentally obtained porosity and the porosity of the adjusted CAD for the all the studied structures (from SP3 to SP19) can be found in Fig. 11. The average difference between the experimental porosity and the adjusted CAD was −1%, allowing to understand that the adopted methodology to modulate the adjusted CAD was efficient.

SLM structures are constructs built layer by layer where in each powder bed the laser will describe a given path and, in this way, define the material areas (in this study named walls), as opposed to the open-cells areas, where the laser was not melting the powder. Some of the

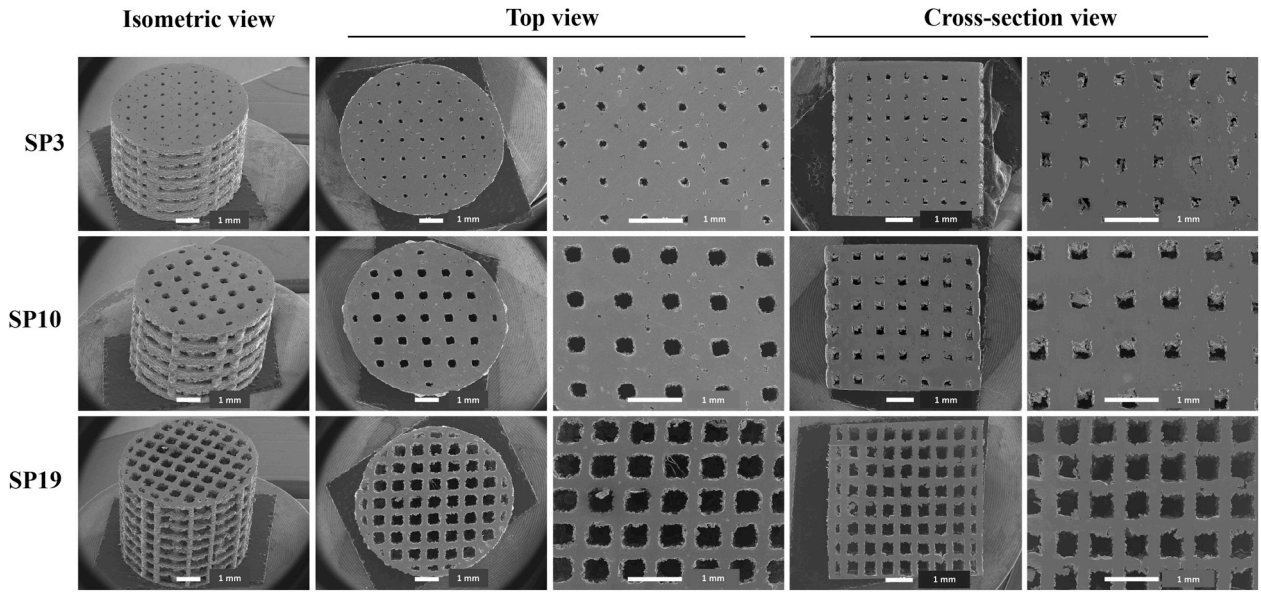

Fig. 8. SEM images of SP3, SP11 and SP19 Ti6Al4V cellular structures.

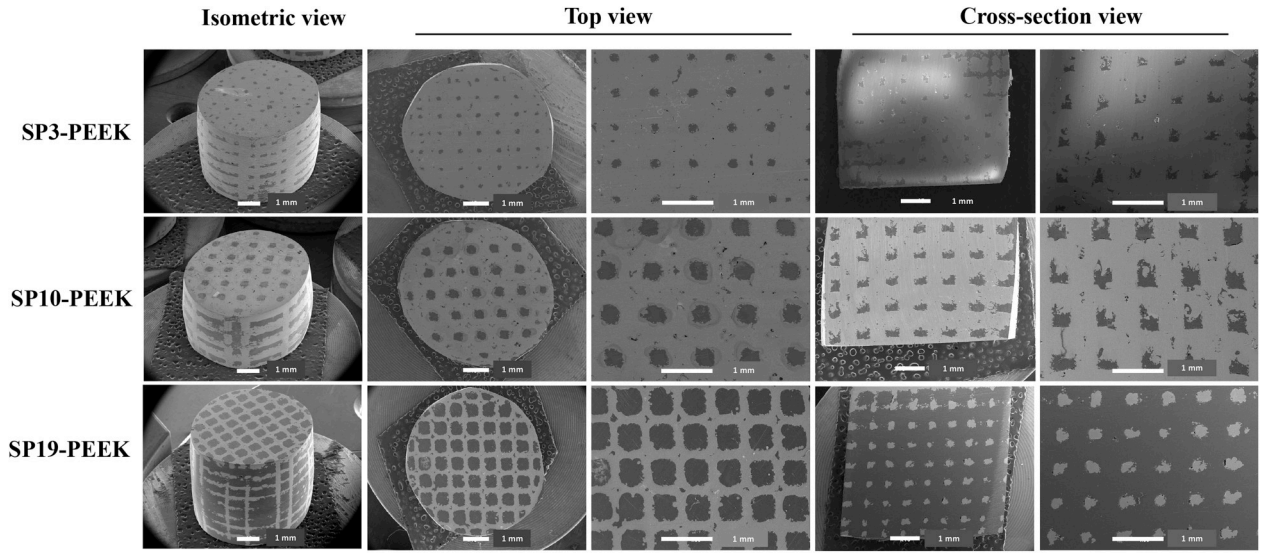

Fig. 9. SEM images of SP3-PEEK, SP11-PEEK and SP19-PEEK multi-material structures.

powder in the vicinity of the laser melted areas, partially melts, contributing to increase the dimensions of the walls and to reduce the open-cells size, when compared to the model CAD. The powder size distribution has a crucial role in this phenomenon, contributing significantly to the detected dimensional and geometrical divergences. Another aspect that is accountable for these differences is inherent to this technology, due to the heat transfer that occurs from the melt pool to the vicinity powder, that is, by this effect, enlarged by melting an additional amount of powders.

In fact, similar deviations between CAD design and SLM produced structures have been reported elsewhere even when using different equipment's and different processing parameters (Yan et al., 2015; Arabnejad et al., 2016; Zhang et al., 2014; Ran et al., 2018; Attar et al., 2015). As an example, Q. Ran et al. (2018) studied 3D printed porous Ti6Al4V implants having open-cells with 500, 700 and 900 μm of diameter (CAD dimensions). In their study, the pore sizes of three types of specimens were consistently lower than the ones of design specifications, having open-cells with 401, 607 and 801 μm of diameter, respectively. These authors reported that these deviations can be explained due to the difference in heat transport between powder and solid material resulting in powder sticking to the surface (Ran et al., 2018).

3.2. Mechanical characterization

3.2.1. Numerical analysis procedure

Mesh convergence analysis were performed for all the structures, aiming to obtain efficient numerical simulations with a number of finite elements correct to avoid singularities on the numerical model and also adequate to avoid needless computational time. Fig. 12 shows some details of an exemplificative numerical analysis (COMSOL Multiphysics) for SP16 and SP16-PEEK structures.

Fig. 12 depicts the Von Mises Stress and displacement distributions for SP16 and SP16-PEEK structures. By analyzing the Von-Mises stress plots, there is a clear indication of normally distributed stresses along the height of the specimen. As expected, the walls intersections,

Table 2
Comparison between the Model CAD details and the produced structures measurements.

Specimen		Model CAD details			Produced structures measurements		
		Open-cells (μm)	Walls (μm)	Porosity[a]/PEEK[b] percentage	Open-cells (μm)	Walls (μm)	Porosity[a]/PEEK[b] percentage
SP1		-	-	~0	-	-	~0
SP2							
SP3[a]	SP3-PEEK[b]	350	400	43.2	232 ± 11	510 ± 9	19.9 ± 0.14
SP4[a]	SP4-PEEK[b]	400	400	46.3	281 ± 10	509 ± 10	23.3 ± 0.73
SP5[a]	SP5-PEEK[b]	350	350	49.9	242 ± 12	448 ± 12	24.0 ± 0.36
SP6[a]	SP6-PEEK[b]	400	350	52.9	285 ± 8	453 ± 11	25.4 ± 0.24
SP7[a]	SP7-PEEK[b]	350	300	53.6	235 ± 6	400 ± 11	25.1 ± 0.40
SP8[a]	SP8-PEEK[b]	450	350	55.9	336 ± 12	454 ± 11	32.4 ± 0.01
SP9[a]	SP9-PEEK[b]	400	300	58.2	293 ± 9	400 ± 11	30.9 ± 0.59
SP10[a]	SP10-PEEK[b]	500	400	58.9	388 ± 10	492 ± 8	33.8 ± 0.46
SP11[a]	SP11-PEEK[b]	500	350	61.7	382 ± 11	453 ± 11	37.9 ± 0.44
SP12[a]	SP12-PEEK[b]	450	300	62.5	331 ± 10	414 ± 11	36.9 ± 0.38
SP13[a]	SP13-PEEK[b]	500	300	65.2	387 ± 10	393 ± 11	40.7 ± 0.18
SP14[a]	SP14-PEEK[b]	600	350	66.7	492 ± 10	464 ± 9	56.5 ± 0.05
SP15[a]	SP15-PEEK[b]	600	300	71.8	490 ± 9	400 ± 13	62.0 ± 0.55
SP16[a]	SP16-PEEK[b]	500	150	83.3	393 ± 6	234 ± 4	68.0 ± 0.44
SP17[a]	SP17-PEEK[b]	600	150	87.0	497 ± 4	240 ± 13	73.3 ± 0.72
SP18[a]	SP18-PEEK[b]	500	100	90.7	398 ± 6	187 ± 12	70.5 ± 0.25
SP19[a]	SP19-PEEK[b]	600	100	92.3	497 ± 14	180 ± 10	78.3 ± 0.01

[a] For Ti6Al4V structures made by SLM.
[b] For Ti6Al4V-PEEK structures made by SLM followed by Pressure Assisted Injection.

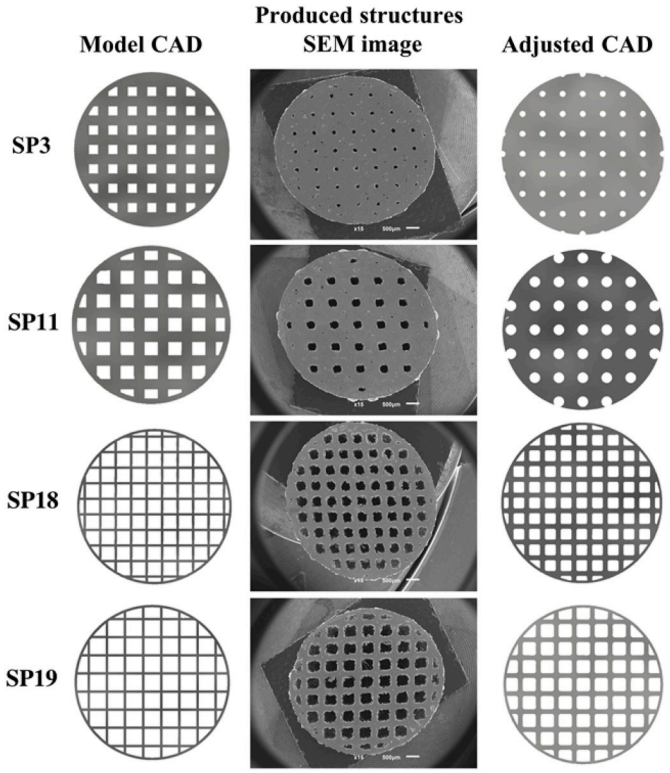

Fig. 10. Model CAD, top view SEM images of the produced specimens and adjusted CAD.

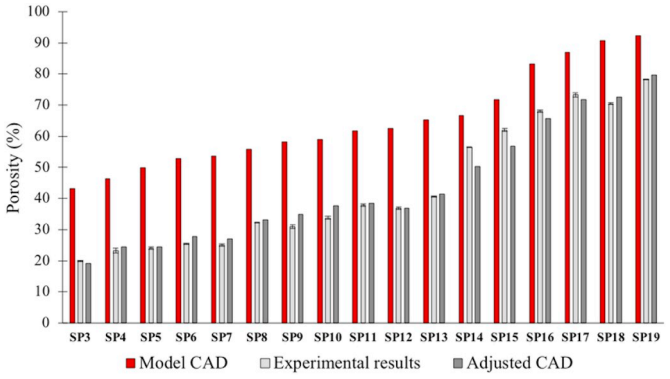

Fig. 11. Porosity values regarding Model CAD, Experimental results (mean values ± standard deviation) and Adjusted CAD.

geometrical discontinuities, exhibit a high stress concentration, displaying the highest stress magnitude. The displacement plots show a homogenous and coherent distribution, indicating no singularities on the model. The numerical stress-strain results exhibited a good agreement when compared to the experimental results.

3.2.2. Experimental and numerical analysis comparison

Fig. 13 shows the relation between the porosity (%) and the elastic modulus (GPa) for the seventeen Ti6Al4V mono-material cellular structures (SP3 to SP19), either regarding the numerical results (model CAD and also adjusted CAD), either regarding the experimental results obtained by performing compression tests.

When analyzing Fig. 13, it can be seen that power law correlations were found between the porosity and the elastic modulus, all of them having a good fitting (Model CAD $R^2 = 0.9141$; Experimental results $R^2 = 0.9356$; Adjusted CAD $R^2 = 0.9450$). The geometrical and dimensional divergences found between the Model CAD and the produced specimens (Table 2) lead to substantial differences on the porosity and on the elastic modulus for all the Ti6Al4V cellular structures (SP3 to SP19).

For the three correlations found in Fig. 13, as expected, lower porosity led to higher values of elastic modulus. Moreover, by comparing the linear functions for the experimental results and for the adjusted CAD numerical a good superposition was found, validating the numerical procedure for the adjusted CAD modulation used in this study.

Fig. 14 shows the correlation between the porosity (%) and the elastic modulus (GPa) for all the Ti6Al4V-PEEK multi-material cellular structures (SP3-PEEK to SP19-PEEK). The power law tendencies for the relations between the porosity and the elastic modulus show a good fit, with R-squared of 0.9473 and 0.9577 for the experimental results and for the adjusted CAD numerical results, respectively. A good superposition was found between the power functions for the experimental results and for the adjusted CAD numerical.

Fig. 15 gathers the results obtained for mono-material Ti6Al4V structures and multi-material Ti6Al4V-PEEK structures and also for the dense specimens (SP1 and SP2), either numerical or experimental.

When analyzing Fig. 15, some aspects can be highlighted. The elastic modulus of the experimental results is on average 148% higher when compared to the model CAD numerical results. This significant difference is related to the above-mentioned dimensional differences between the CAD design and the as-produced specimens. These differences, as seen in Fig. 11, substantially influence the porosity obtained on the produced specimens, leading to higher elastic modulus. Particularly, SP16, SP17, SP18 and SP19 exhibit the highest relative differences on the elastic modulus between the experimental and the numerical (Model CAD) results, with 197, 181, 244 and 229% higher elastic modulus, respectively. In fact, all the produced specimens exhibit lower open-cells sizes (lowering around 112 μm) and higher wall sizes (increasing around 100 μm), however these dimensional dissimilarities had a higher percent effect on the elastic modulus of SP16, SP17, SP18 and SP19 specimens, once these specimen's CAD walls sizes were the minimum values (100 and 150 μm) obtained. All the multi-material Ti6Al4V- PEEK cellular structures exhibit a higher elastic modulus when compared to the corresponding mono-material Ti6Al4V cellular structure. When analyzing the effect of the introduction of PEEK into the open-cells, i.e., when comparing the experimental results of the mono-material and the multi-material specimens an average increase of 4.82 GPa on the elastic modulus was found.

As reported by F. Melo-Fonseca et al. (2018), Ti6Al4V-based cellular structures can be used on implants, such as, hip prosthesis. As previously referred, these structures can be designed to have a specific elastic modulus that suits each patient bone properties that can be obtained by tomography or magnetic resonance imaging 3D data (Chen and Thouas, 2015; Yan et al., 2015; Ryan et al., 2006; Thavornyutikarn et al., 2014). In this regard, Fig. 15 highlights (yellow area) the suitable specimens that owe an elastic modulus similar to that of natural cortical bone (≈20 GPa) (Wang et al., 2016; Chen et al., 2017; Fousová et al., 2017; Bose et al., 2018), that allow reducing stress shielding and bone resorption (Geetha et al., 2009; Holzwarth and Cotogno, 2012; Dallago et al., 2018).

In fact, by using SLM technique, customized Ti6Al4V cellular implants can be fabricated to exhibit a required mechanical behavior/compromise between implant material and bone. Moreover, it is well known that living bone tissue is a self-optimizing structure that adapts to external loading conditions. According to Frost's mechanostat theory, its biological response depends on the level of strain exerted (Frost, 2004). Piccinini et al. (2016) identified the octahedral shear strain as the most relevant strain for the mechanostat theory, as follows:

$$\varepsilon_{oct} = \frac{2}{3} \times \sqrt{(\varepsilon_1 - \varepsilon_2)^2 + (\varepsilon_2 - \varepsilon_3)^2 + (\varepsilon_3 - \varepsilon_1)^2} \quad (2)$$

in which ε_i corresponds to the ith principal value of the continuum

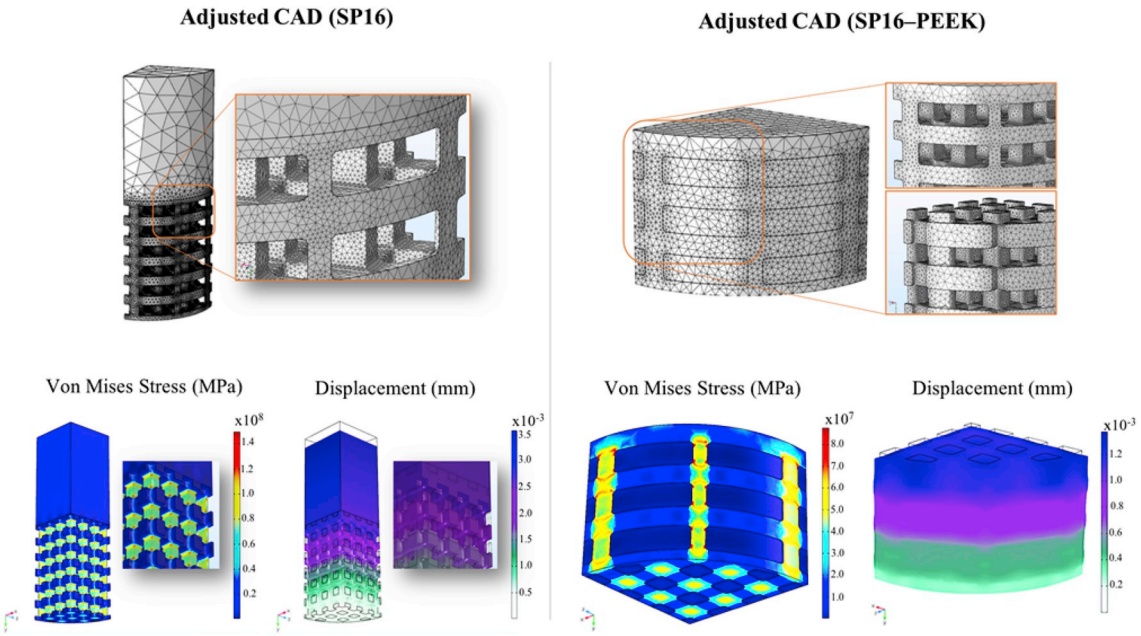

Fig. 12. Mesh and distribution of Von Mises Stress and displacement for SP16 and SP16-PEEK.

strain tensor ε.

The mechanostat theory defines five main ranges of strain:

- Below 1000 με - disuse bone atrophy (stress shielding)
- Between 1000 and 1500 με - bone homoeostasis is maintained (adapted state)
- Between 1500 and 3000 με) – bone modeling takes place, increasing the bone mass due to the physiologic demand (physiological overload)
- Above 3000 με - bone damage and absorption (pathologic overload)
- Higher than 25,000 με - bone fracture upon reaching the bone ultimate strength

The compression tests results showed that mono-material Ti6Al4V SP16 structure displays an elastic modulus close to that of cortical bone (18.4 GPa - experimental result and 19.1 GPa - numerical result). Besides the elastic modulus, the octahedral shear strain is an important aspect that defines the bone-implant suitable transference of stress. In this sense, SP16 structure adjusted CAD was used to estimate the octahedral shear strain for different ranges of stress. Mechanostat theory does not consider fluid flow which is a very important parameter. In this sense, the numerical study here presented can only be considered for static cases. Fig. 16 shows the octahedral shear strain distribution of mono-material Ti6Al4V SP16 for different loading conditions. Load values of 95, 345, 655 and 905N, corresponding to compression stresses of 14, 49, 93 and 128 MPa respectively, were used on the analysis. These loading values were selected based on literature considering the loading range reported for single-led stance, walking, running and jumping, respectively (Tomar, 2009; Shah et al., 2012; Bayraktar et al., 2004; Trabelsi et al., 2011; Mughal et al., 2015).

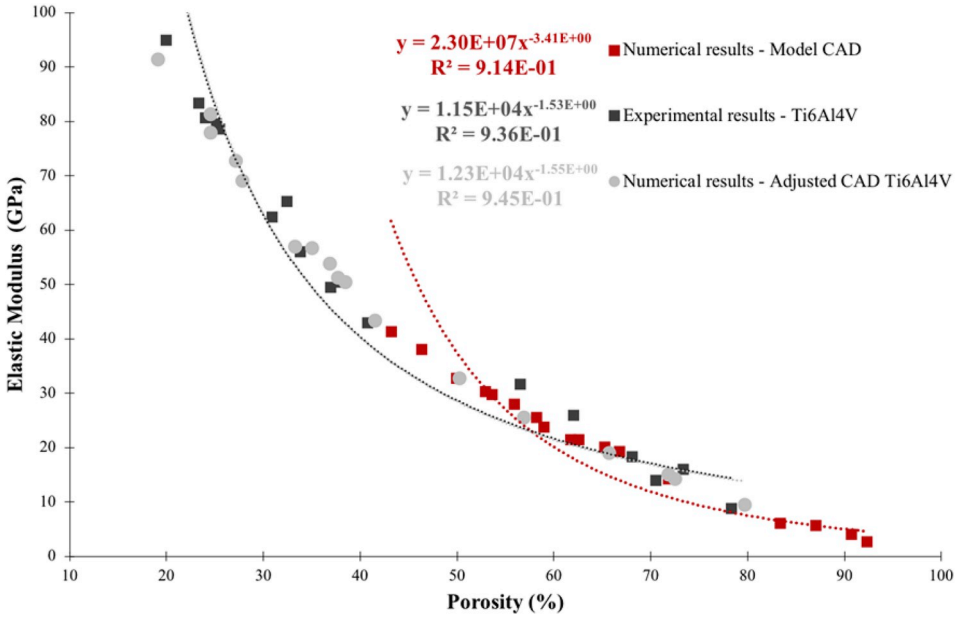

Fig. 13. Relation between the porosity and the elastic modulus for the Ti6Al4V mono-material cellular structures.

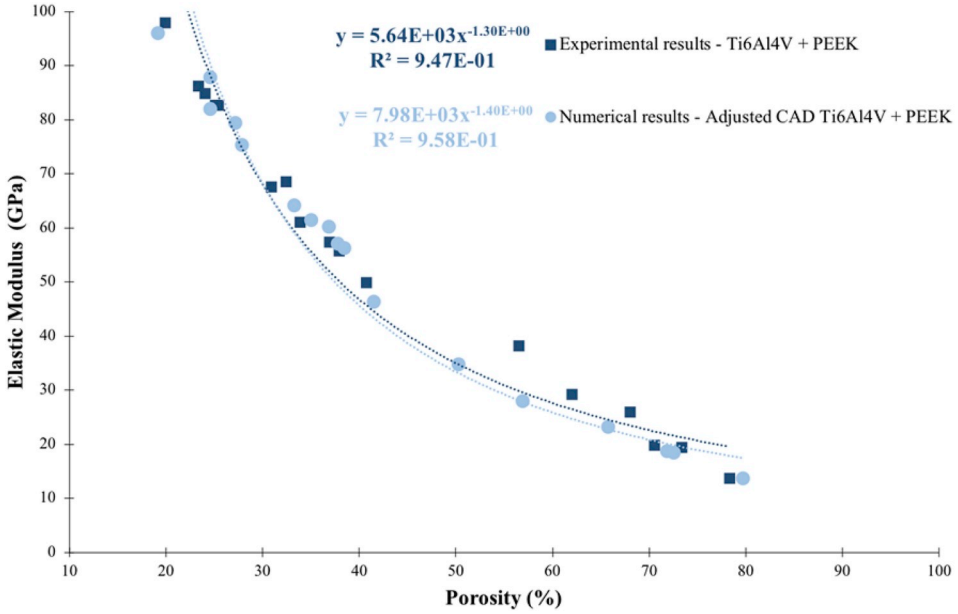

Fig. 14. Relation between the porosity and the elastic modulus for the Ti6Al4V-PEEK multi-material cellular structures.

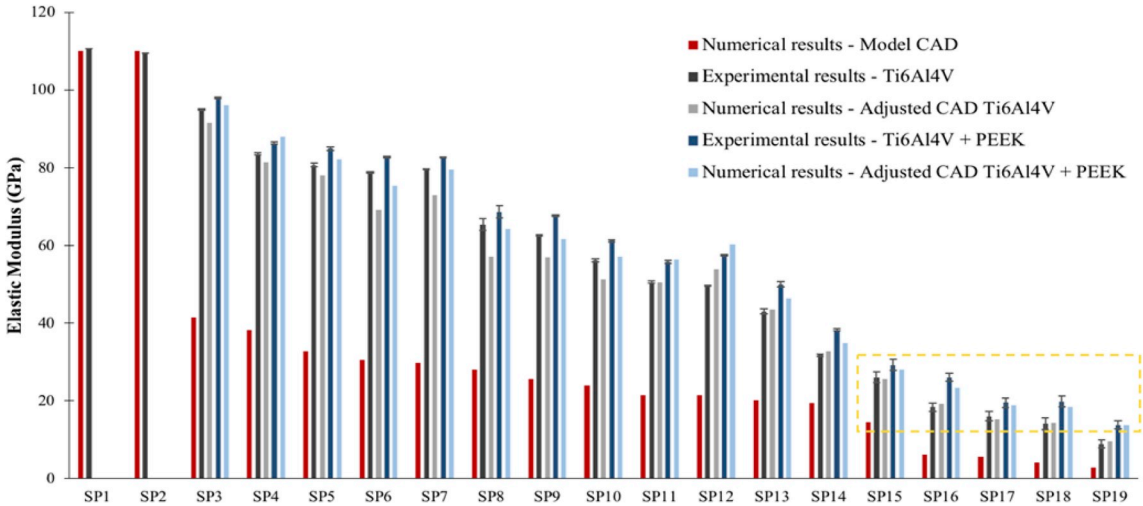

Fig. 15. Resume of the elastic modulus values obtained for the numerical and the experimental results for all the specimens investigated.

Fig. 16 exemplifies the four types of loading conditions mentioned above, with the intent of assessing the adequacy of a hip implant owing SP16 structure, regarding their elastic behavior (strain) compliance with natural bone. Fig. 16 shows that for a compression stress of 14 MPa a maximum shear strain of 2040 was obtained, corresponding to simple standing. For an applied stress of 49 MPa (walking regime), a significant area of the structure displays a microstrain varying from 1500 to 3000, being this within the physiological overload (that leads to increase bone mass). For this stress level, corresponding to walking activity, the mechanostat theory indicates that this structure exhibits a shear strain that can promote bone modeling. In this sense, for this stress level, besides a suitable elastic modulus, SP16 exhibits a suitable shear strain, indicating that this structure can be used to obtain an effective implant-bone stress transference and in this way reducing stress shielding. For a compression stress of 93 and 128 MPa, maximum microstrains higher than 10,000 are obtained. In fact, a maximum value of 20,000 microstrain was obtained for 128 MPa. According to the mechanostat theory these values are in the range of pathologic overload and can lead to bone damage or even fracture. For an applied stress of this amplitude, an implant having this structure would potentially lead to the bone damage (considering bone yield strength (≈120 MPa) (Bayraktar et al., 2004)) or even fracture.

Considering the large diversity of implants, there may be implants or even zones of an implant that have different requirements, however, they require similar elastic properties. While in some areas the resistance to wear is of particular importance, in other areas, the presence of open-cells which allow bone ingrowth can be desired for improved anchorage and implant success. The multi-material structures can be suitable for the first scenario (SP19-PEEK for instance) and mono-material Ti6Al4V for the second circumstance being able to respond to different requirements existing in different areas of the implant. As an example, SP16 can be pointed as a suitable structure to apply in implant materials once display an elastic modulus close to cortical bone and also displays octahedral shear microstrain in the mechanostat range that can promote bone modeling.

3.3. Predictive models for the dimensions, the porosity and the elastic modulus

In this study, cubic-like Ti6Al4V cellular structures were produced

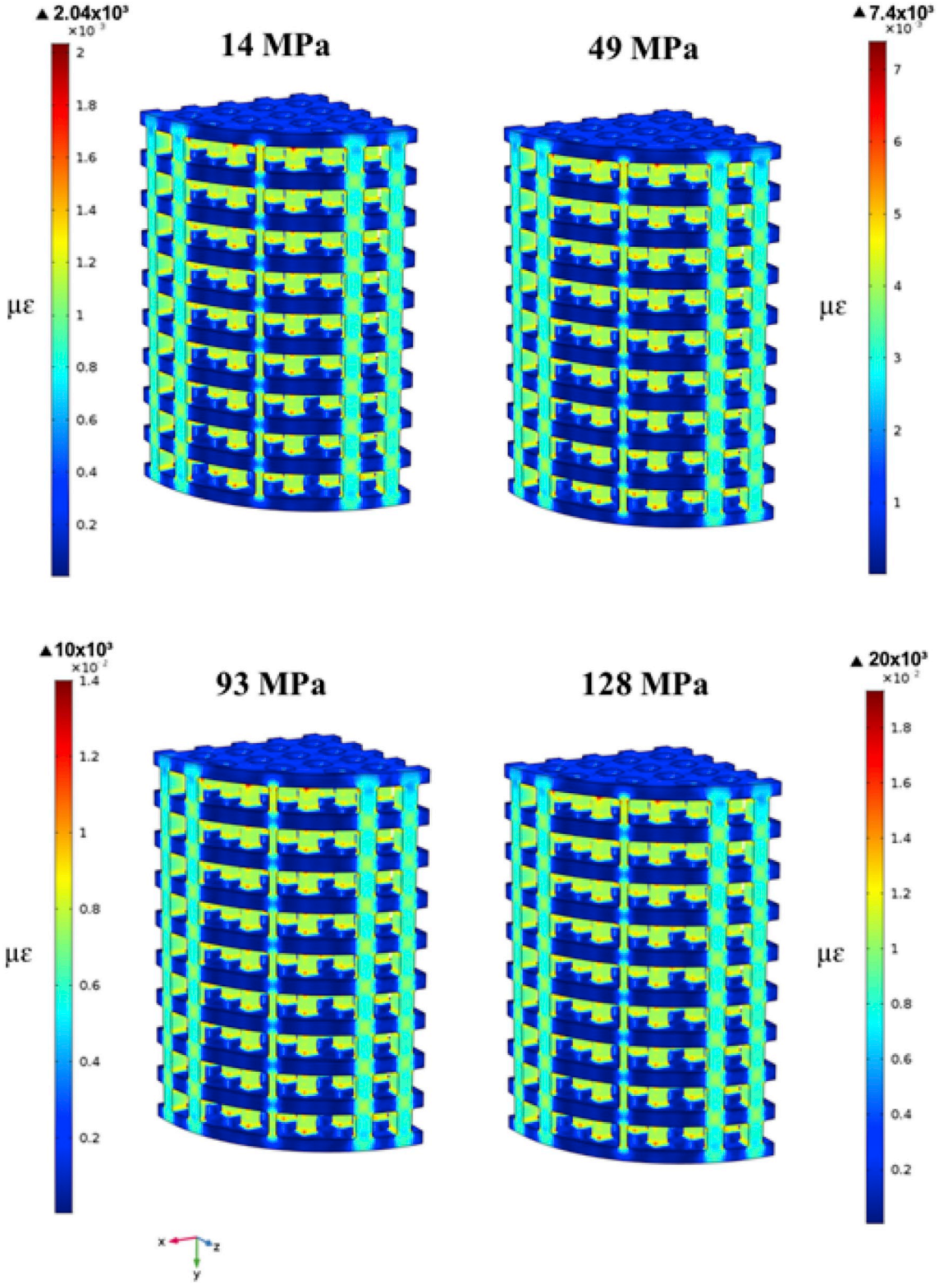

Fig. 16. SP16 structure octahedral shear strains distribution for different loading conditions.

using a SLM 125HL commercial equipment. As mentioned before, the Ti6Al4V cellular structures were modelled with quadrangular open-cells and the distance between two consecutive open-cells being defined as walls. Figs. 17 and 18 show the correlations between the CAD porosity and the measured porosity and also the correlation between the open-cell and wall sizes when comparing the CAD design and the produced Ti6Al4V cellular structures measurements.

As depicted in Figs. 17 and 18, correlation models having R^2 of 0.9462 for the porosity, 0.9973 for the open-cell size and 0.9965 for the wall sizes were obtained. The determined liner correlations exhibit high coefficients of determination indicating that the observed differences occurring between the CAD design and the produced specimens have a constant trend.

These aspects show that these dimensional deviations are in fact

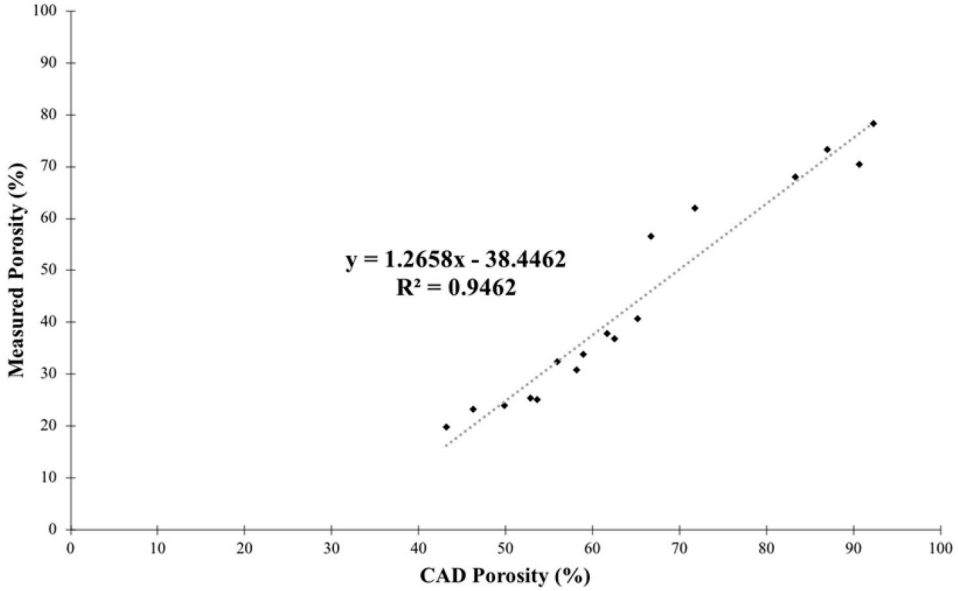

Fig. 17. Correlation models to predict the porosity of cubic-like Ti6Al4V cellular structures as function of the model CAD design.

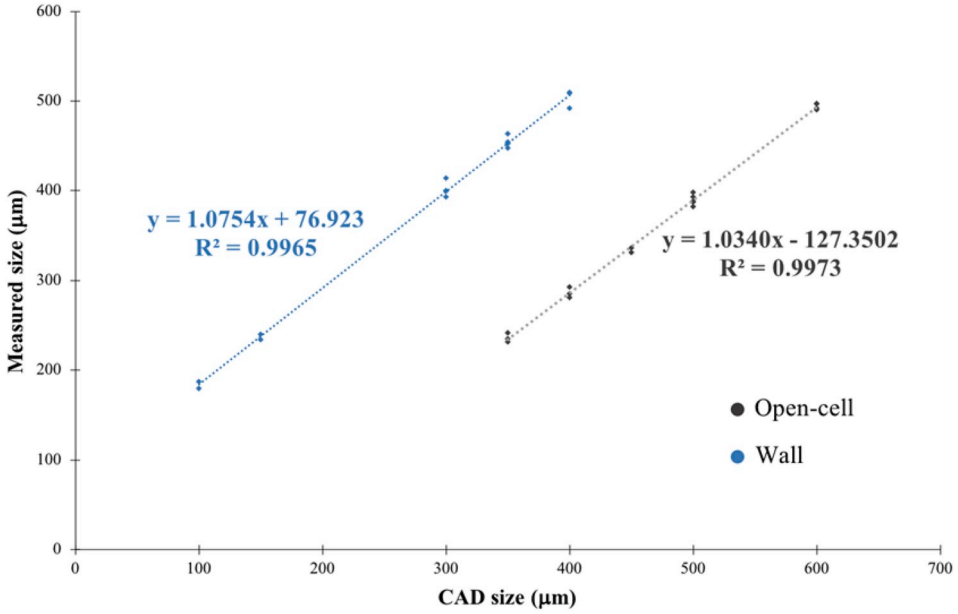

Fig. 18. Correlation models to predict the real dimensions of cubic-like Ti6Al4V cellular structures as function of the model CAD design.

inherent to SLM fabrication, being found for different dimensional ranges, but above all empowers the need and the importance of developing predictive tools that can be used by engineers to design and obtain near-net shape Ti6Al4V cubic-like specimens matching the physical and mechanical requirements. In this sense, for the mono-material Ti6Al4V cellular structures, it was obtained a mathematical relationship between the elastic modulus and the CAD design open-cell and wall size. Equation (3) ($R^2 = 0.9893$) presents the experimental elastic modulus as a function of the open-cell and wall sizes (CAD design) follows:

$$E_{mono-material} = 42.9965 - 0.1847\,x + 0.4751\,y + 1.8181 \times 10^{-4}x^2 - 5.9294 \times 10^{-3}xy - 6.6636 \times 10^{-5}\,y^2 \quad (3)$$

where x is the open-cell size (µm) and y corresponds to wall size (µm) of the CAD design.

When regarding the multi-material Ti6Al4V-PEEK cubic-like structures results, the ensuing linear, equation (4) ($R^2 = 0.9925$), estimates the experimental elastic modulus as a function of the open-cell and wall sizes (CAD design) for the multi-material Ti6Al4V-PEEK cellular structures, as follows:

$$E_{multi-material} = 39.7205 - 0.1217\,x + 0.4415\,y + 9.4232 \times 10^{-5}x^2 - 5.1581 \times 10^{-4}xy - 8.6838 \times 10^{-5}\,y^2 \quad (4)$$

The present study aims to be a useful tool to predict the dissimilarities, typically detected on cubic-like Ti6Al4V structures produced by SLM, when compared to the model CAD design but especially help the engineer to design and fabricate structures that present small deviations to the intended elastic modulus. By predicting these dimensional and geometrical dissimilarities it is possible to design a customized implant that exhibits a required/desired porosity and mechanical behavior. For instance, a hip implant can be designed having regions with open-cells for bone ingrowth combined with PEEK-filled cells, both of them placed in specific locations throughout the implant, suiting specific local requirements.

4. Conclusions

- Mono-material Ti6Al4V and multi-material Ti6Al4V-PEEK cellular structures were produced by SLM and SLM followed by Pressure Assisted Injection, respectively;
- The differences between the model CAD design and the SLM-produced Ti6Al4V structures were systematically measured by image analysis;
- Adjusted CAD designs were modelled reproducing the dimensions and the geometries of the SLM-produced Ti6Al4V structures;
- Mathematical models were obtained to predict the real dimensions, porosity and elastic modulus of biomaterial Ti6Al4V-based structures
- Predictive models are proposed to help engineers to design and obtain near-net shape Ti6Al4V and Ti6Al4V-PEEK structures matching the desired geometry, dimension, porosity and elastic modulus; .
- The designed AM structures exhibit a strain and elastic modulus that complies with that of bone, thus being optimum solutions for bone modeling on orthopedic implants.

Cofinanciado por:
COMPETE 2020 PORTUGAL 2020 UNIÃO EUROPEIA Fundo Europeu de Desenvolvimento Regional FCT Fundação para a Ciência e a Tecnologia MINISTÉRIO DA EDUCAÇÃO E CIÊNCIA

Acknowledgements

This work was supported by FCT (Fundação para a Ciência e a Tecnologia) through the grant SFRH/BD/128657/2017, the projects PTDC/EMS-TEC/5422/2014_ADAPTPROSTHESIS, POCI-01-0145-FEDER-030353 (SMARTCUT), NORTE 010145_FEDER-000018-HAMaBICo and UID/EEA/04436/2019.

References

Arabnejad, S., Johnston, R.B., Ann, J., Singh, B., Tanzer, M., Pasini, D., 2016. High-strength porous biomaterials for bone replacement : a strategy to assess the interplay between cell morphology , mechanical properties , bone ingrowth and manufacturing constraints. Acta Biomater. 30, 345–356. https://doi.org/10.1016/j.actbio.2015.10.048.

Ashby, M.F., 2006. The properties of foams and lattices. Philos. Trans. R. Soc. A Math. Phys. Eng. Sci. 364, 15–30. https://doi.org/10.1098/rsta.2005.1678.

Attar, H., Löber, L., Funk, A., Calin, M., Zhang, L.C., Prashanth, K.G., Scudino, S., Zhang, Y.S., Eckert, J., 2015. Mechanical behavior of porous commercially pure Ti and Ti-TiB composite materials manufactured by selective laser melting. Mater. Sci. Eng. A 625, 350–356. https://doi.org/10.1016/j.msea.2014.12.036.

Bagheri, Z.S., Melancon, D., Liu, L., Johnston, R.B., Pasini, D., 2017. Compensation strategy to reduce geometry and mechanics mismatches in porous biomaterials built with selective laser melting. J. Mech. Behav. Biomed. Mater. 70, 17–27. https://doi.org/10.1016/j.jmbbm.2016.04.041.

Bartolomeu, F., Faria, S., Carvalho, O., Pinto, E., Alves, N., Silva, F.S., Miranda, G., 2016. Predictive models for physical and mechanical properties of Ti6Al4V produced by selective laser melting. Mater. Sci. Eng. A 663, 181–192. https://doi.org/10.1016/j.msea.2016.03.113.

Bartolomeu, F., Buciumeanu, M., Pinto, E., Alves, N., Carvalho, O., Silva, F.S., Miranda, G., 2017a. 316L stainless steel mechanical and tribological behavior—a comparison between selective laser melting, hot pressing and conventional casting. Addit. Manuf. 16, 81–89. https://doi.org/10.1016/j.addma.2017.05.007.

Bartolomeu, F., Sampaio, M., Carvalho, O., Pinto, E., Alves, N., Gomes, J.R., Silva, F.S., Miranda, G., 2017b. Tribological behavior of Ti6Al4V cellular structures produced by selective laser melting. J. Mech. Behav. Biomed. Mater. 69, 128–134. https://doi.org/10.1016/j.jmbbm.2017.01.004.

Bartolomeu, F., Buciumeanu, M., Pinto, E., Alves, N., Silva, F.S., Carvalho, O., Miranda, G., 2017c. Wear behavior of Ti6Al4V biomedical alloys processed by selective laser melting, hot pressing and conventional casting. Trans. Nonferrous Met. Soc. China (English Ed). 27, 829–838. https://doi.org/10.1016/S1003-6326(17)60060-8.

Bartolomeu, F., Costa, M.M., Gomes, J.R., Alves, N., Abreu, C.S., Silva, F.S., Miranda, G., 2018a. Implant surface design for improved implant stability – a study on Ti6Al4V dense and cellular structures produced by selective laser melting. Tribol. Int. https://doi.org/10.1016/j.triboint.2018.08.012.

Bartolomeu, F., Buciumeanu, M., Costa, M.M., Gasik, M., Silva, F.S., Miranda, G., 2018b. Multi-material Ti6Al4V & PEEK cellular structures produced by Selective Laser Melting and Hot Pressing: a tribocorrosion study targeting orthopedic applications. J. Mech. Behav. Biomed. Mater. https://doi.org/10.1016/j.jmbbm.2018.09.009.

Bayraktar, H.H., Morgan, E.F., Niebur, G.L., Morris, G.E., Wong, E.K., Keaveny, T.M., 2004. Comparison of the elastic and yield properties of human femoral trabecular and cortical bone tissue. J. Biomech. 37, 27–35. https://doi.org/10.1016/S0021-9290(03)00257-4.

Bobbert, F.S.L., Lietaert, K., Eftekhari, A.A., Pouran, B., Ahmadi, S.M., Weinans, H., Zadpoor, A.A., 2017. Acta Biomaterialia Additively manufactured metallic porous biomaterials based on minimal surfaces : a unique combination of topological , mechanical , and mass transport properties. Acta Biomater. 53, 572–584. https://doi.org/10.1016/j.actbio.2017.02.024.

Bose, S., Ke, D., Sahasrabudhe, H., Bandyopadhyay, A., 2018. Progress in materials science additive manufacturing of biomaterials. Prog. Mater. Sci. 93, 45–111. https://doi.org/10.1016/j.pmatsci.2017.08.003.

Buciumeanu, M., Almeida, S., Bartolomeu, F., Costa, M.M., Alves, N., Silva, F.S., Miranda, G., 2018. Ti6Al4V cellular structures impregnated with biomedical PEEK - new material design for improved tribological behavior. Tribol. Int. 119, 157–164. https://doi.org/10.1016/j.triboint.2017.10.038.

Chen, Q., Thouas, G.A., 2015. Metallic implant biomaterials. Mater. Sci. Eng. R Rep. 87, 1–57. https://doi.org/10.1016/j.mser.2014.10.001.

Chen, S.Y., Huang, J.C., Pan, C.T., Lin, C.H., Yang, T.L., Huang, Y.S., Ou, C.H., Chen, L.Y., Lin, D.Y., Lin, H.K., Li, T.H., Jang, J.S.C., Yang, C.C., 2017. Microstructure and Mechanical Properties of Open-Cell Porous Ti-6Al- 4V Fabricated by Selective Laser Melting, vol. 713. pp. 248–254. https://doi.org/10.1016/j.jallcom.2017.04.190.

Dai, N., Zhang, L.-C., Zhang, J., Chen, Q., Wu, M., 2016. Corrosion behavior of selective laser melted Ti-6Al-4V alloy in NaCl solution. Corros. Sci. 102, 484–489. https://doi.org/10.1016/j.corsci.2015.10.041.

Dallago, M., Fontanari, V., Torresani, E., Leoni, M., Pederzolli, C., Potrich, C., Benedetti, M., 2018. Fatigue and biological properties of Ti-6Al-4V ELI cellular structures with variously arranged cubic cells made by selective laser melting. J. Mech. Behav. Biomed. Mater. 78, 381–394. https://doi.org/10.1016/j.jmbbm.2017.11.044.

Dias, M.R., Guedes, J.M., Flanagan, C.L., Hollister, S.J., Fernandes, P.R., 2014. Medical Engineering & Physics Optimization of scaffold design for bone tissue engineering . A Comput. Exp. Study 36, 448–457.

Fousová, M., Vojt, D., Jablonská, E., Fojt, J., 2017. Characteristics of gradient porosity Ti-6Al-4V alloy prepared by SLM process. J. Mech. Behav. Biomed. Mater. Promising 69, 368–376. https://doi.org/10.1016/j.jmbbm.2017.01.043.

Frost, H.M., 2004. A 2003 update of bone physiology and Wolff s law for clinicians. Angle Orthod. 74, 3–15.

Garcia-Gonzalez, D., Rodriguez-Millan, M., Rusinek, A., Arias, A., 2015. Low temperature effect on impact energy absorption capability of PEEK composites. Compos. Struct. 134, 440–449. https://doi.org/10.1016/j.compstruct.2015.08.090.

Geetha, M., Singh, A.K., Asokamani, R., Gogia, A.K., 2009. Ti based biomaterials, the ultimate choice for orthopaedic implants - a review. Prog. Mater. Sci. 54, 397–425. https://doi.org/10.1016/j.pmatsci.2008.06.004.

Holzwarth, U., Cotogno, G., 2012. Total hip arthroplasty - state of the art, challenges and prospects. J. Bone Jt. Surg. https://doi.org/10.2788/31286.

Koike, H., Kida, K., Santos, E.C., Rozwadowska, J., Kashima, Y., Kanemasu, K., 2012. Tribology International Self-lubrication of PEEK polymer bearings in rolling contact fatigue under radial loads. Tribiology Int. 49, 30–38. https://doi.org/10.1016/j.triboint.2011.12.005.

Kurtz, S.M., Devine, J.N., 2007. PEEK Biomaterials in Trauma, Orthopedic , and Spinal Implants. 28. pp. 4845–4869. https://doi.org/10.1016/j.biomaterials.2007.07.013.

Melo-Fonseca, F., Lima, R., Costa, M.M., Bartolomeu, F., Alves, N., Miranda, A., Gasik, M., Silva, F.S., Silva, N.A., Miranda, G., 2018. 45S5 BAG-Ti6Al4V structures: the influence of the design on some of the physical and chemical interactions that drive cellular response. Mater. Des. 160, 95–105. https://doi.org/10.1016/j.matdes.2018.08.056.

Moura, C.G., Pereira, R., Buciumeanu, M., Carvalho, O., Bartolomeu, F., Nascimento, R., Silva, F.S., 2017. Effect of laser surface texturing on primary stability and surface properties of zirconia implants. Ceram. Int. 43, 15227–15236. https://doi.org/10.1016/j.ceramint.2017.08.058.

Mughal, U.N., Khawaja, H.A., Moatamedi, M., 2015. Finite element analysis of human femur bone. Int. J. Multiphys. 9, 101–108. https://doi.org/10.1260/1750-9548.9.2.101.

Piccinini, M., Cugnoni, J., Botsis, J., Ammann, P., Wiskott, A., 2016. Numerical prediction of peri-implant bone adaptation: comparison of mechanical stimuli and sensitivity to modeling parameters. Med. Eng. Phys. 38, 1348–1359. https://doi.org/10.1016/j.medengphy.2016.08.008.

Ran, Q., Yang, W., Hu, Y., Shen, X., Yu, Y., Xiang, Y., Cai, K., 2018. Osteogenesis of 3D printed porous Ti6Al4V implants with different pore sizes. J. Mech. Behav. Biomed. Mater. 84, 1–11. https://doi.org/10.1016/j.jmbbm.2018.04.010.

Rotta, G., Seramak, T., 2015. Estimation of Young's Modulus of the Porous Titanium Alloy with the Use of Fem Package. https://doi.org/10.1515/adms-2015-0020.

Ryan, G., Pandit, A., Apatsidis, D.P., 2006. Fabrication methods of porous metals for use in orthopaedic applications. Biomaterials 27, 2651–2670. https://doi.org/10.1016/j.biomaterials.2005.12.002.

Sampaio, M., Buciumeanu, M., Henriques, B., Silva, F.S., Souza, J.C.M., Gomes, J.R., 2016. Tribocorrosion behavior of veneering biomedical PEEK to Ti6Al4V structures. J. Mech. Behav. Biomed. Mater. 54, 123–130. https://doi.org/10.1016/j.jmbbm.2015.09.010.

Shah, S., Bougherara, H., Schemitsch, E.H., Zdero, R., 2012. Biomechanical stress maps of an artificial femur obtained using a new infrared thermography technique validated

by strain gages. Med. Eng. Phys. 34, 1496–1502. https://doi.org/10.1016/j.medengphy.2012.02.012.
Stamp, R., Fox, P., O'Neill, W., Jones, E., Sutcliffe, C., 2009. The development of a scanning strategy for the manufacture of porous biomaterials by selective laser melting. J. Mater. Sci. Mater. Med. 20, 1839–1848. https://doi.org/10.1007/s10856-009-3763-8.
Thavornyutikarn, B., Chantarapanich, N., Chen, Q., 2014. Bone Tissue Engineering Scaffolding : Computer-Aided Scaffolding Techniques. https://doi.org/10.1007/s40204-014-0026-7.
Tomar, V., 2009. Insights into the effects of tensile and compressive loadings on micro-structure dependent fracture of trabecular bone. Eng. Fract. Mech. 76, 884–897. https://doi.org/10.1016/j.engfracmech.2008.12.013.
Trabelsi, N., Yosibash, Z., Wutte, C., Augat, P., Eberle, S., 2011. Patient-specific finite element analysis of the human femur-A double-blinded biomechanical validation. J. Biomech. 44, 1666–1672. https://doi.org/10.1016/j.jbiomech.2011.03.024.
Van Hooreweder, B., Apers, Y., Lietaert, K., Kruth, J.P., 2017. Improving the fatigue performance of porous metallic biomaterials produced by selective laser melting. Acta Biomater. 47, 193–202. https://doi.org/10.1016/j.actbio.2016.10.005.
Wang, X., Xu, S., Zhou, S., Xu, W., Leary, M., Choong, P., Qian, M., Brandt, M., Xie, Y.M., 2016. Topological design and additive manufacturing of porous metals for bone scaffolds and orthopaedic implants: a review. Biomaterials 83, 127–141. https://doi.org/10.1016/j.biomaterials.2016.01.012.
Weißmann, V., Bader, R., Hansmann, H., Laufer, N., 2016. Influence of the structural orientation on the mechanical properties of selective laser melted Ti6Al4V open-porous scaffolds. Mater. Des. 95, 188–197. https://doi.org/10.1016/j.matdes.2016.01.095.
Xu, Y., Zhang, D., Zhou, Y., Wang, W., Cao, X., 2017. Study on topology optimization design, manufacturability, and performance evaluation of Ti-6Al-4V porous structures fabricated by selective laser melting (SLM). Materials 10. https://doi.org/10.3390/ma10091048.
Yan, C., Hao, L., Hussein, A., Raymont, D., 2012. Evaluations of cellular lattice structures manufactured using selective laser melting. Int. J. Mach. Tool Manuf. 62, 32–38. https://doi.org/10.1016/j.ijmachtools.2012.06.002.
Yan, C., Hao, L., Hussein, A., Young, P., 2015. Ti-6Al-4V triply periodic minimal surface structures for bone implants fabricated via selective laser melting. J. Mech. Behav. Biomed. Mater. 51, 61–73. https://doi.org/10.1016/j.jmbbm.2015.06.024.
Zhang, S., Wei, Q., Cheng, L., Li, S., Shi, Y., 2014. Effects of Scan Line Spacing on Pore Characteristics and Mechanical Properties of Porous Ti6Al4V Implants Fabricated by Selective Laser Melting, vol. 63. pp. 185–193. https://doi.org/10.1016/j.matdes.2014.05.021.